

THE ROLE OF THE RADIAL ORBIT INSTABILITY IN DARK MATTER HALO FORMATION AND STRUCTURE

JILLIAN M. BELLOVARY¹, JULIANNE J. DALCANTON¹, ARIF BABUL², THOMAS R. QUINN¹, RYAN W. MAAS¹, CRYSTAL G. AUSTIN³, LILIYA L. R. WILLIAMS³, AND ERIC I. BARNES⁴

Draft version November 20, 2018

ABSTRACT

For a decade, N-body simulations have revealed a nearly universal dark matter density profile, which appears to be robust to changes in the overall density of the universe and the underlying power spectrum. Despite its universality, the physical origin of this profile has not yet been well understood. Semi-analytic models by Barnes et al. (2005) have suggested that the density structure of dark matter halos is determined by the onset of the radial orbit instability (ROI). We have tested this hypothesis using N-body simulations of collapsing dark matter halos with a variety of initial conditions. For dynamically cold initial conditions, the resulting halo structures are triaxial in shape, due to the mild aspect of the instability. We examine how variations in initial velocity dispersion affect the onset of the instability, and find that an isotropic velocity dispersion can suppress the ROI entirely, while a purely radial dispersion does not. The quantity σ^2/v_c^2 is a criterion for instability, where regions with $\sigma^2/v_c^2 \lesssim 1$ become triaxial due to the ROI or other perturbations. We also find that the radial orbit instability sets a scale length at which the velocity dispersion changes rapidly from isotropic to radially anisotropic. This scale length is proportional to the radius at which the density profile changes shape, as is the case in the semi-analytic models; however, the coefficient of proportionality is different by a factor of ~ 2.5 . We conclude that the radial orbit instability is likely to be a key physical mechanism responsible for the nearly universal profiles of simulated dark matter halos.

Subject headings: dark matter — galaxies:halos — galaxies:formation — galaxies:evolution — instabilities

1. INTRODUCTION

The universal density profile of dark matter halos has been widely observed in cosmological N-body simulations (Cole & Lacey 1996; Moore et al. 1999; Bullock et al. 2001; van den Bosch 2002; Navarro et al. 2004); however, the physical origins are not yet understood. Whether formed in an isolated collapse or by hierarchical merging, dark matter halo density profiles have a characteristic double-power law shape. This shape is usually discussed in terms of the slope of the density profile $\gamma \equiv d(\log \rho)/d(\log r)$. The canonical halo profile has $\gamma \sim -1$ in the inner regions and $\gamma \sim -3$ in the outer regions (Dubinski & Carlberg 1991; Navarro et al. 1996, 1997; Huss et al. 1999; MacMillan et al. 2006). While there are disagreements on the exact values of γ , the halo density profiles appear to be similar over decades in radius. There is also evidence that such profiles may accurately fit the luminous parts of early-type galaxies as well (Dalcanton & Hogan 2001; Merritt et al. 2005).

Within dark matter halos, quantities other than density show universal profiles as well. For example, Taylor & Navarro (2001) and later Dehnen & McLaughlin (2005) showed that the phase-space density, represented by ρ/σ^3 , has a constant

power-law slope of $\alpha \sim 1.9$ for over two and a half decades in radius in spite of a varying density profile (see also Austin et al. (2005) for an analytic exploration of this behavior). There is also evidence for a universality in the relation between the slope of the density profile and the velocity anisotropy. The anisotropy parameter, β is defined as

$$\beta \equiv 1 - \sigma_\phi^2/2\sigma_r^2, \quad (1)$$

where σ_ϕ is the velocity dispersion in the tangential direction and σ_r is the velocity dispersion in the radial direction. β describes the degree of anisotropy of the velocity dispersion in a spherical halo, which in simulations ranges from isotropic in the core ($\beta = 0$) to radially anisotropic at the outskirts ($\beta = 1$) (Cole & Lacey 1996; Carlberg et al. 1997; Fukushige & Makino 2001). Hansen & Moore (2006) find a direct correlation between β and the density profile slope for halos with a wide variety of initial conditions (i.e. isolated collapse, mergers). Hansen et al. (2006) find another universality, this time in the velocity distribution function, for a similar variety of initial conditions.

The radial orbit instability (ROI) may be the cause of the apparent universality of these dark matter halo properties. The ROI occurs in anisotropic spherical systems composed of particles with predominantly radial orbits. The instability arises when particles in precessing elongated loop orbits experience a torque due to a slight asymmetry. This torque causes them to lose some angular momentum and move towards the center of the system. Particles with small enough angular momenta become trapped in box orbits, aligning them-

Electronic address: jillian@astro.washington.edu

¹ Department of Astronomy, University of Washington, Seattle, WA

² Department of Physics and Astronomy, University of Victoria, Victoria, BC, Canada

³ Department of Astronomy, University of Minnesota, Minneapolis, MN

⁴ Department of Physics, University of Wisconsin – La Crosse, La Crosse, WI

selves with the growing bar and reinforcing the initial perturbation. As a result, the halo becomes triaxial in shape. This phenomenon has been examined in detail by Dejonghe & Merritt (1988) using N-body simulations, by Weinberg (1991) using linear analysis, and by Huss et al. (1999) and MacMillan et al. (2006) for the specific case of isolated dark matter halo collapse. These groups find that the onset of the ROI corresponds to a flattening of the central density cusp of the halo, and may be responsible for the double power-law shape of the halo. The ROI is reviewed in Merritt (1999; §6.2).

Semi-analytic models have also been used to examine the spherical collapse of dark matter halos, beginning with Gunn & Gott (1972). These models (Gott 1975; Gunn 1977; Bertschinger 1985) include only radial motions and produce single power-law density profiles. When non-radial motions are included, halo density profiles range from power-laws (Ryden & Gunn 1987) to NFW-like (Hiotelis 2002; Le Delliou & Henriksen 2003; Ascasibar et al. 2004). Recently, however, Barnes et al. (2005) extended the semi-analytic model of Williams et al. (2004) to include a physical representation of the ROI. The resulting halos have a double power-law density slope similar to those of N-body simulations. Barnes et al. (2005) concluded that the density scale length and the anisotropy radius are correlated, and that the ROI is directly responsible for the shape of the density profile. While Barnes et al. (2005)’s work is suggestive, the complexities of a dynamical instability are not easily captured by analytic or semi-analytic techniques. We therefore turn to studying the link between the ROI and halo structure by using high resolution N-body simulations.

In this paper, we examine in detail the effect of random motions on the onset of the ROI and the final structure of collapsed dark matter halos, and attempt to verify the relation between the scale length and the anisotropy radius reported by Barnes et al. (2005). We analyze a set of N-body simulations of isolated, collapsing dark matter halos with a variety of initial velocity dispersions to study the evolution of halo properties. Considering a range of velocity dispersions allows us to suppress the ROI in some cases, helping us to isolate its physical effects. In §2 we describe our simulations and show that they are robust to resolution and softening effects. We describe the properties of the halos in §3, including the shape and anisotropy evolution, the effects of velocity dispersion, and the scale-length – anisotropy radius relation. We summarize our results in §4.

2. SIMULATIONS

We performed simulations using PKDGRAV (Stadel 2001; Wadsley et al. 2004), a parallel KD Tree gravity solver. The initial system is an isolated, spherical halo with a Gaussian radial density profile, mimicking an over-density in the early universe. All particles are given Hubble flow velocities, such that the halo is initially expanding. We evolve the system in physical coordinates for 12.8 Gyr, which was set to allow 83% of the mass of the halo to collapse by the present time; this corresponds to a starting redshift of ~ 12 according to the most recent results from WMAP (Spergel et al. 2007).

We ran several simulations with comparable density profiles but with a range of initial velocity dispersions,

allowing us to estimate the threshold at which the ROI will occur. In principle, a dynamically “warmer” system should resist the ROI (Merritt & Aguilar 1985), since any perturbations will be washed out by the tangential velocity dispersions. We assigned initial random velocities (σ) to the particles assuming a Gaussian distribution with a mean of zero; these numbers are then added to the existing Hubble flow velocities. The amplitudes of these initial velocity dispersions were 1σ , 2σ , and 3σ , where σ is 18% of the circular velocity at the virial radius of the final system. Simulations with a higher velocity dispersion are too warm to collapse at all. We also carried out simulations with no velocity dispersion, at both standard and high resolution. Finally, we attempted to isolate the importance of tangential velocity dispersions by carrying out a simulation with a pure radial initial velocity dispersion of 3σ . Table 1 lists the initial value of the ratio $-2T/W$ (see §3.3) for each simulation for a more intuitive grasp of the value of each σ .

In addition to various velocity dispersions, we ran simulations with a range of softenings and particle resolutions. Our highest resolution simulation has over 2.8 million particles, while the simulations testing the effects of velocity dispersion have about one fifth of that number. These standard-resolution simulations are comparable in number of particles to MacMillan et al. (2006), but are much larger than the simulations in Huss et al. (1999), which have $\sim 10,000$ particles within the virial radius of each halo. The softening, ϵ , was set to 0.054 times r_{200} of the final collapsed halo, and is the same for all simulations. Time steps were set to an accuracy criterion proportional to $\eta\sqrt{\epsilon/a}$ where $\eta = 0.2$ is the timestep criterion and a is the acceleration of a particle (Wadsley et al. 2004). We use a force accuracy criterion of 0.55. A summary of all simulations is in Table 1.

2.1. Resolution and Softening Tests

Figure 1 shows how the structure of our simulated halos are affected by particle number (also referred to in the text as resolution). The top panels show the density profile for the fully evolved, 0σ halo at standard resolution (left) and at high resolution (right). Each profile is fit with a NFW profile (purple dotted line) and a Navarro et al. (2004) profile (also known as an Einasto profile) (red dashed line). The profiles for the two runs are similar over a large range in radius. However, as can be seen by the residuals from the fits, the standard resolution simulation does not adequately model the inner core of the halo ($r < 0.05r_{200}$, where we define r_{200} as the virial radius in which the enclosed density is 200 times the critical density of the universe. There is also a difference in the innermost cores when looking at the $z = 0$ axis ratio profiles (Fig. 1, middle panels). The high-resolution run (right) shows a somewhat more triaxial core, particularly at the center. However, the anisotropy and phase-space density profiles show no significant differences between the two simulations (Fig. 1, bottom panels, left and right, respectively). We analyze these profiles in more detail in §3. The bulk of the difference between the two resolutions is apparent only within $\sim 0.05 \times r_{200}$. Outside of this radius our medium-resolution simulations are robust to resolution effects, while inside this radius the profiles may be less

TABLE 1
SIMULATION PROPERTIES

Simulation	# particles	Velocity Dispersion ^a	Softening ^b	Initial -2T/W
V0_H	2865813	0	1	1.44
V0_M	573302	0	1	1.45
V1_M	573302	1	1	1.49
V2_M	573302	2	1	1.59
V3_M	573302	3	1	1.64
V3r_M	573302	3 (radial only)	1	1.87
V0_M_S1	573302	0	2	1.45
V0_M_S2	573302	0	0.5	1.45

^a in units of σ , where σ is 18% of the circular velocity of the “cold” standard-resolution halo at $z = 0$.

^b in units of 0.054 times r_{200} of the “cold” standard-resolution halo at $z = 0$.

certain, and biased towards shallow density profiles and rounder shapes.

We have also tested the impact of gravitational softening on our simulations. We performed two simulations, identical to the standard-resolution, 0σ halo but with softening increased/decreased by a factor of two. Decreasing the softening length does not noticeably change any important quantities (density, velocity dispersion, axis ratios, phase-space density). Increasing the softening length results in a shallower core density profile, due to the decreased gravitational force at small inter-particle distances. The phase-space density profile is similarly affected by the softening changes; however, the anisotropy profile shows no difference when the softening lengths are changed. These effects are only noticeable within a radius of $0.05r_{200}$, the same radius within which we may be affected by resolution limitations ($0.054r_{200}$). We conclude that our results are robust beyond a radius of $0.05r_{200}$. This distance corresponds to 10 kpc for a Milky Way-size halo.

3. RESULTS

As the halo collapses, we measure the density profile, velocity dispersion tensor, and the axis ratios as a function of radius at each time step. We expect to see higher central densities and larger radial velocity dispersions with increasing time. However, if the ROI is present we also expect to see deviations from spherical symmetry develop in regions with large radial velocity dispersions. These deviations would be accompanied by increasing tangential velocities due to the additional torques.

3.1. Axis Ratios

The most obvious evidence for the ROI is the growth of triaxiality in the shape of the halo. We see this behavior clearly in our simulations. We measure axis ratios as a function of radius by dividing the halo into 196 equal particle-number radial bins based on particle density, and then calculating the moment-of-inertia tensor for each bin (see Babul & Starkman (1992) for an application of this method). The square root of the ratios of the principal moments of inertia in the directions of the three axes of symmetry give the axis ratios of the particles within each radial bin. This method more accurately tracks the radial variations of the axis ratios than methods which analyze all particles interior to a given radius. This latter method is always dominated by the shape of the inner halo, where the majority of the virialized halo’s

mass is located, and thus is insensitive to variations in the axis ratios at large radii.

After 0.6 Gyr, the first shell⁵ reaches the center leading to a large radial velocity dispersion. In response, a triaxial structure develops in the core of the halo. The resulting axis ratio profiles can be seen in Figure 2, which portrays the evolution of the axis ratios b/a and c/a at a range of timesteps for the high-resolution, zero velocity dispersion halo. The center of the halo quickly becomes triaxial and remains so throughout the collapse. The triaxiality is fairly prolate ($c \sim 0.72b$) and appears as a central bar. The outer edges of the halo have yet to collapse, and so remain spherical. As the collapse progresses, the triaxial region of the halo grows outwards, and eventually the majority of the halo settles to an equilibrium b/a ratio of ~ 0.6 .

If the formation of the triaxial bar in Figure 2 is due to the ROI, then it should be suppressed when the orbits are less radial. Our simulations with larger isotropic initial velocity dispersions would then be expected to show weaker triaxiality. The particles in these simulations have larger tangential velocities, which increases the typical angular momentum of particles’ orbits, suppressing the formation of box orbits, and thus decreasing the strength of the ROI. Figure 3 shows the resulting fully evolved axis ratio profiles for a series of simulations with increasing initial random velocities. The standard and high resolution runs with zero velocity dispersion show the central triaxial signature of the ROI. The 1σ halo also shows some of this structure, but with a rounder core; this halo appears to undergo a weak form of the ROI. The 2σ and 3σ halos, on the other hand, remain nearly spherical throughout until the end of their evolution. Their final shapes are characterized by rather spherical cores, with the inner axis ratios becoming progressively more spherical with increasing initial tangential velocities. A pre-existing isotropic velocity distribution therefore prevents the onset of self-gravitating instabilities such as the ROI. Our results are supported by Trenti & Bertin (2006), who find that an isotropic core acts to stabilize a radially collapsing system against the ROI, even when the halo is highly anisotropic overall. Although we do not show the full time evolution, the halos that develop a strong or moderate ROI do so quickly, establishing a prolate triaxial core within 1 Gyr of the

⁵ While N-body halos do not have specific “shells” like those in the semi-analytic models, we use this terminology here to refer to particles at a similar initial radius and gravitational potential.

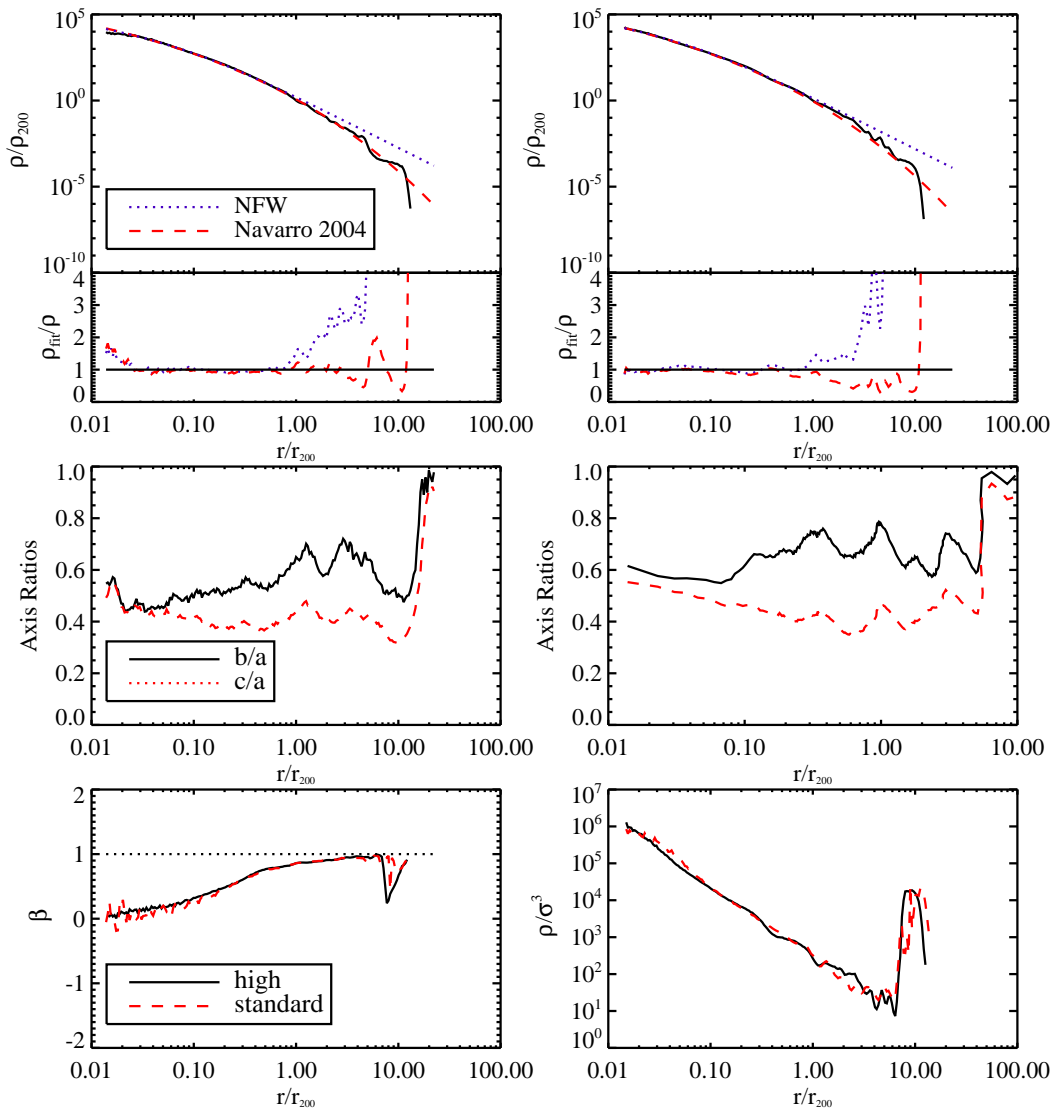


FIG. 1.— Comparison of the standard- and high-resolution fully evolved halos. *Top row:* Density profiles of the standard resolution run (left) and the high resolution run (right). Fits are NFW with a concentration of 14.6 (purple dotted line) and the Einasto profile with $\alpha = 0.2$ (red dashed line). The residuals depict the superior core-fitting in the high-resolution simulation and also show that the Einasto profile is a good fit to $r \sim 10r_{200}$. *Middle row:* Axis ratio profiles for the standard run (left) and the high-res run (right). Black line is b/a , and red dashed line is c/a . *Bottom left:* Anisotropy profiles for the standard (red dashed) and high-res (black solid) simulations. *Bottom right:* phase-space density profiles for the standard (red dashed) and high-res (black solid) runs. The standard resolution run shows slight deviations in density profile at $r < 0.05r_{200}$ and is slightly less triaxial. However, the anisotropy and phase-space density profiles are similar at high and standard resolutions.

onset of collapse. Thus the triaxial shape indicates the presence of an instability; a phenomenon such as random scattering of the particles off of the potential would not create any preferred shape.

We note that the increase in radial velocity dispersion alone has no significant effect on the final shape of the halo compared to the 0σ collapse. In the bottom right panel of Figure 3, we plot results for a simulation with large initial radial velocity dispersions, but no tangential velocities. Physically, the increased initial velocity dispersion does little to change the final radial velocity dispersion of the core, since the latter is dominated by the larger radial motions produced by the gravitational collapse of the halo as a whole. Thus, the resulting axis ratio profile is nearly identical to the case with no initial velocity dispersion. The only significant difference is a

slight delay in the collapse of the outer regions.

To determine the physical likelihood of having velocity dispersions as high as that in the 3σ halo, we compared our N-body simulations to the semi-analytic model of Williams et al. (2004), which treats an evolving perturbation as a series of gravitationally interacting shells. The model includes the effects of nearby substructure, which imparts a velocity dispersion onto the collapsing shells. This velocity dispersion increases with time, as the local substructure becomes more developed and a shell's time of exposure to the substructure increases. In contrast, in our N-body simulations of isolated collapsing halos the velocity dispersions are assigned only at the outset.

The semi-analytic model shows that a velocity dispersion of 2σ is given to a shell detaching from the Hubble

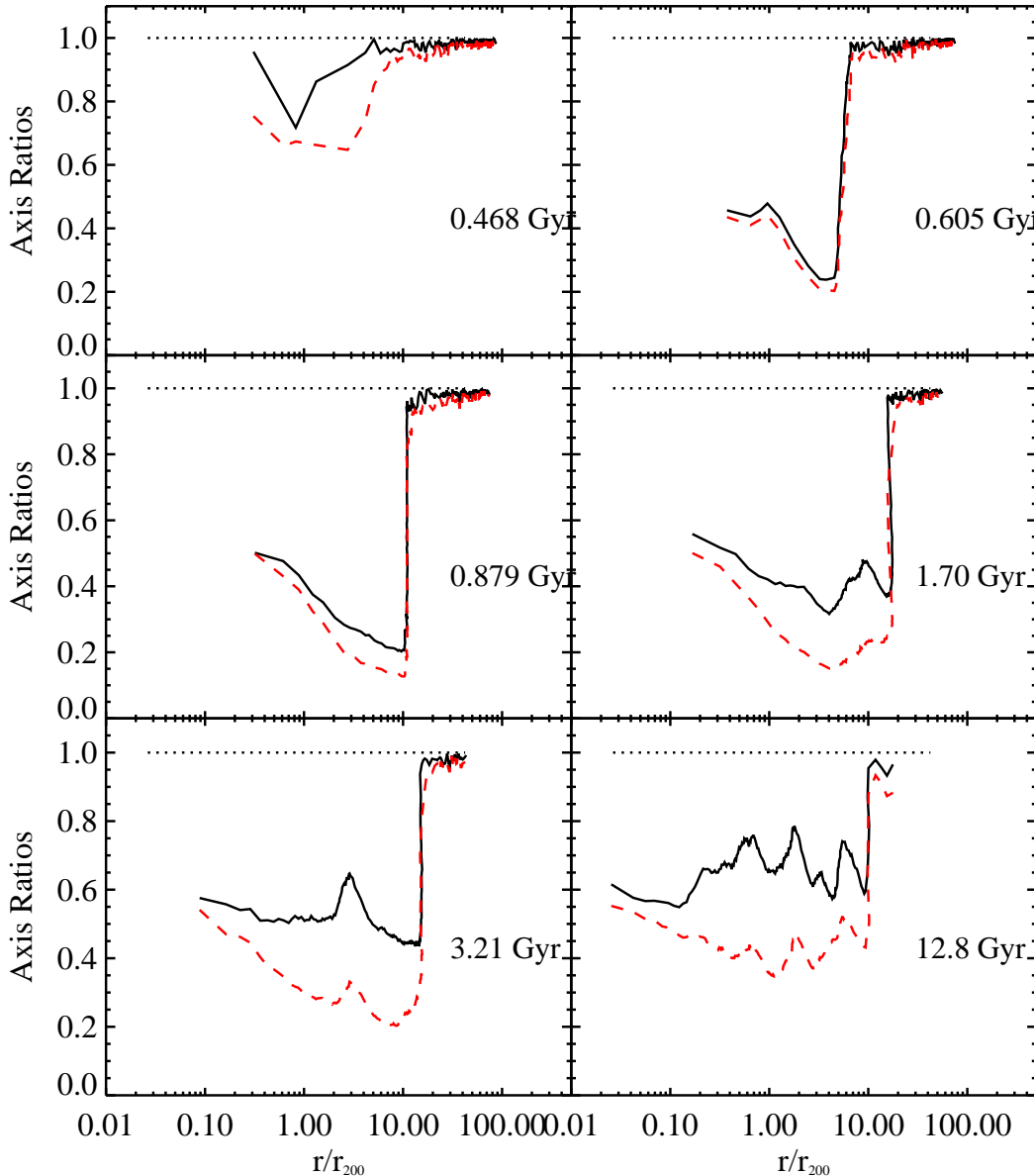


FIG. 2.— Axis ratio profiles of the highest resolution halo at various times. Black solid lines are the ratio b/a , red dashed lines are the ratio c/a . The halo profiles quickly become prolate in the inner regions, with the prolate region expanding to larger radii with increasing time. The profiles are normalized to r_{200} at each timestep. We interpret the various “bumps” in the profiles as being crossing shells that have not yet reached equilibrium.

flow at a redshift of 6.7, while 3σ is assigned to a shell at $z \sim 4.3$. These redshifts correspond to times when the ROI is occurring or has just occurred in the 0σ N-body simulations; at these times the innermost particles’ motions are dominated by the gravitational potential of the halo and will not be strongly affected by external torques due to substructure. Subsequent infalling particles will have increased velocity dispersion due to these effects of substructure; however, the ROI will have already produced a triaxial core at this point.

To summarize, the particles which collapse first and undergo the ROI may be slightly affected by torques due to substructure, but these forces are not strong enough to cause the large velocity dispersions which quench the ROI. In addition, our 2σ and 3σ halos which do not undergo the ROI are not physically plausible, since the lo-

cal substructure cannot impart such large torques on the innermost particles at the early times at which they collapse. This suggests that in a cosmological context, the ROI will have time to operate in the central regions, before cosmological torques have a significant effect.

3.2. Velocity Dispersion Evolution

If the ROI is responsible for the triaxiality in the inner regions of low velocity dispersion halos (Figure 3), then we should expect the onset and radial extent of the triaxiality to be associated with regions of highly anisotropic radial velocity dispersions and growing tangential velocities. For our simulations, we calculate σ_r and σ_ϕ at each timestep using 196 spherical bins. Velocity dispersions are determined by subtracting the average bulk velocity from the velocities in each bin.

In Figures 4 and 5 we show the radial variation of the

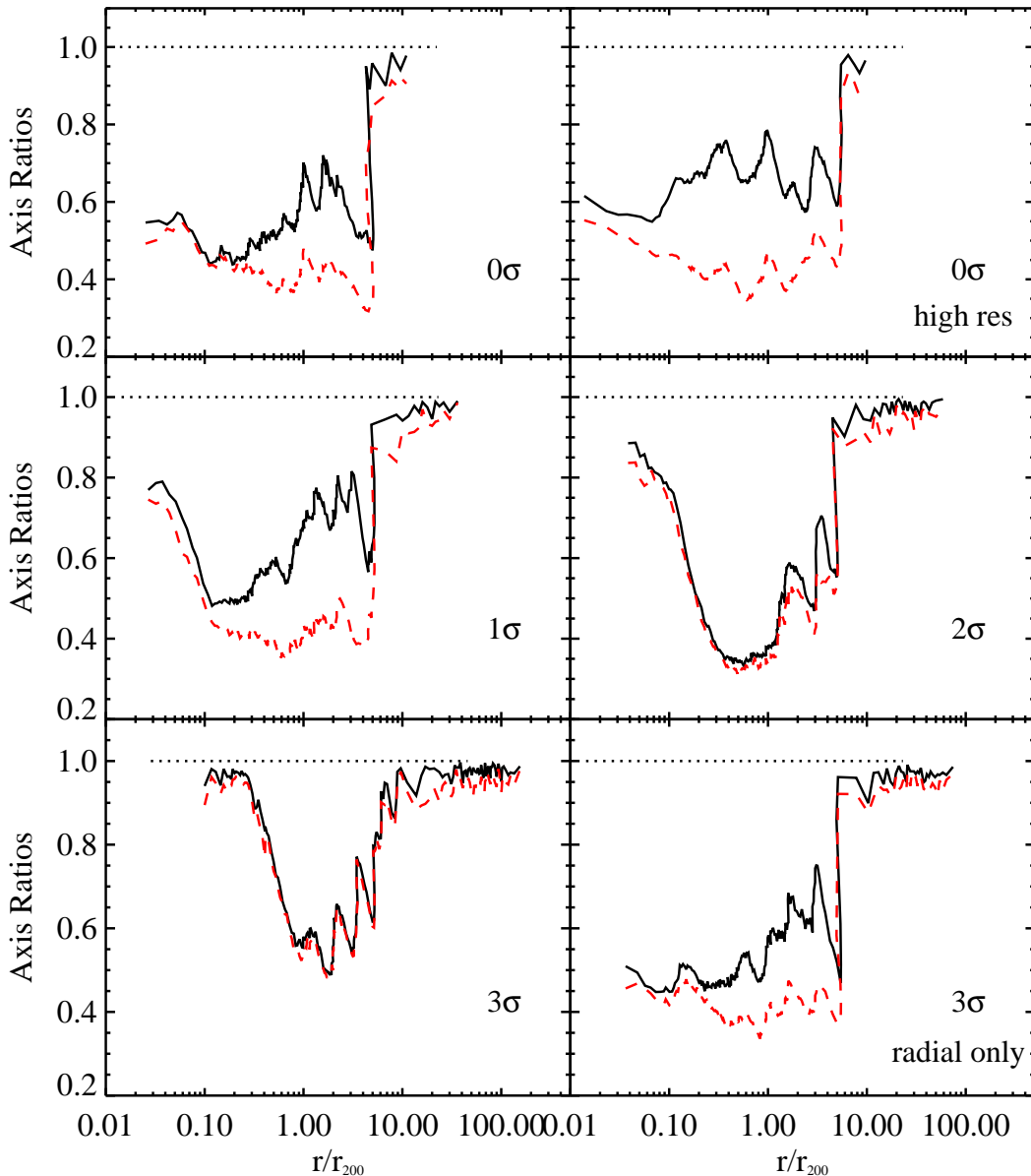


FIG. 3.— The final axis ratio profiles of each simulation. Black solid lines are the ratio b/a , red dashed lines are the ratio c/a . As the velocity dispersion is increased, the halo becomes increasingly spherical in the inner regions ($r \lesssim 0.2r_{200}$), suppressing the ROI.

radial and tangential velocity dispersions as a function of time for our different halos. The central radial velocity dispersion of the 0σ halo undergoes a sharp increase as the innermost regions collapse into the center of the halo (Figure 4, upper right panel, black solid line). The radial velocity dispersion increases outward with time as the halo collapses and material from larger radii falls inward and virializes. The 1σ halo (red dotted line) undergoes a slower collapse and thus the jump in σ_r is delayed. The slower collapse is due to the larger dynamical pressure support provided by the additional initial velocity dispersion. However, despite these initial variations in collapse times, after a few billion years every halo has collapsed and virialized, and all of the σ_r profiles become nearly indistinguishable. This likeness is not surprising considering the similarities in the final density and other profiles (see §3.4, 3.5).

The tangential velocity dispersion also shows an in-

crease in the center of each halo early in the evolution (Figure 5). In the case of the 0σ halo, this increase is due to the torques applied by the radial orbit instability. In the halos which do not undergo the ROI, σ_ϕ still increases due to the increased mass in the center of the halo, as the cores grow from material infalling from large radii. This increase in the central mass will cause any orbiting particles to migrate inwards due to the larger gravitational forces. However, as the particles move inwards, their angular velocity must increase to conserve angular momentum. Thus, halos with high initial σ_ϕ can *also* increase their tangential velocity dispersion, even when the ROI does not operate. This effect will also contribute to increasing σ_ϕ in the 0σ halo once the ROI has imparted net angular momentum to some of the particles. As with the radial velocity dispersion, the final tangential velocity dispersions are very similar for each halo, even though the mechanisms to create such profiles are differ-

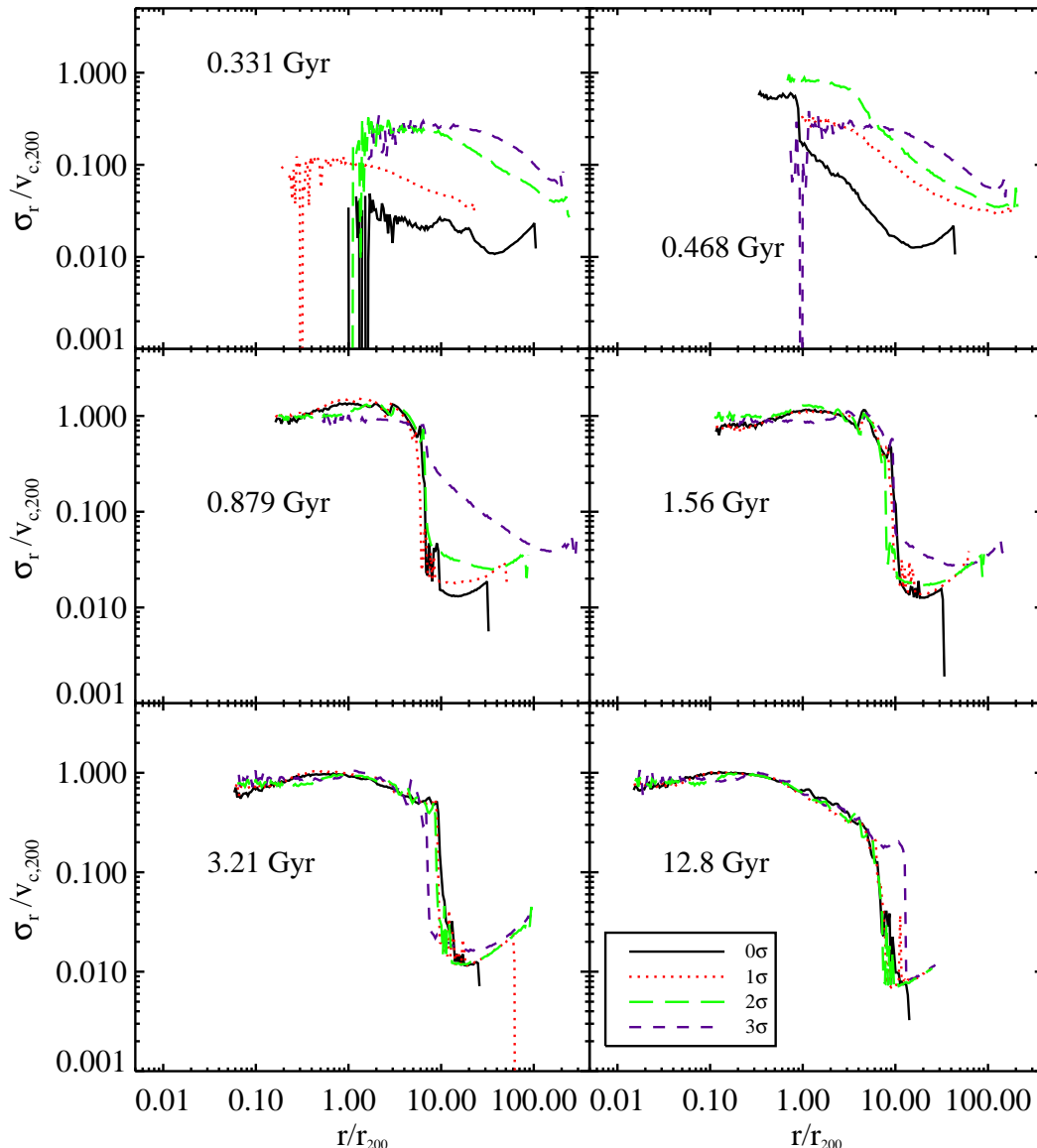


FIG. 4.— The evolution of the radial velocity dispersion profile for each of the halos. Simulations represented are no dispersion (black solid line), 1σ dispersion (red dotted line), 2σ dispersion (green long-dashed line), and the 3σ dispersion (purple dashed line). The timestep is labelled on each panel. Initially, σ_r is a small fraction of the final virial velocity. As the system virializes, however, $\sigma_r/v_{c,200}$ tends to approach unity. The virialization clearly occurs from the inside out.

ent, and the resulting halos have different shapes. The similarity suggests that after the ROI initially increases σ_ϕ , all subsequent evolution is set by angular momentum conservation during collapse. Therefore, while the ROI does not uniquely create the observed universal halo properties such as the NFW density profile, it does play a crucial role in seeding the initial tangential velocities in the dynamically “cold” collapse case, which then set the subsequent evolution of the halo.

Armed with the velocity dispersion evolution shown in Figures 4 and 5, we now return to the origin of the triaxiality seen for *all* halos in Figure 3 (i.e. in the inner regions of the 0σ and 1σ halos, and the outer regions of the 2σ and 3σ halos). In Figure 6 we plot the ratio of the square of the velocity dispersion over the circular velocity at a given radius. When the velocity dispersions are less than the circular velocity (i.e. $\sigma^2/v_c^2 < 1$), halos become unstable to triaxial perturbations. If a slight

perturbation occurs, the tangential velocity dispersion is not sufficient to wash out the perturbation in less than an orbital time. This is the case at early times for the 0σ and 1σ halos in the inner regions, as well as in the outer regions for the 2σ and 3σ halos. Where this mismatch of velocity scales occurs, any triaxial perturbation will grow until the ratio of σ^2/v_c^2 approaches unity. Comparing Figure 6 to Figure 3 shows that indeed the outer prolateness seen in the high- σ halos begins at the radius where σ^2/v_c^2 drops below 1. Interior to this point, the velocity dispersions are high enough that any triaxiality is smoothed out by random motions before it can be reinforced. In the low- σ halos, σ^2/v_c^2 starts well below 1, but the ROI acts quickly to raise the velocity dispersions of the centers of the halos, resulting in triaxial cores.

3.3. Global Anisotropy

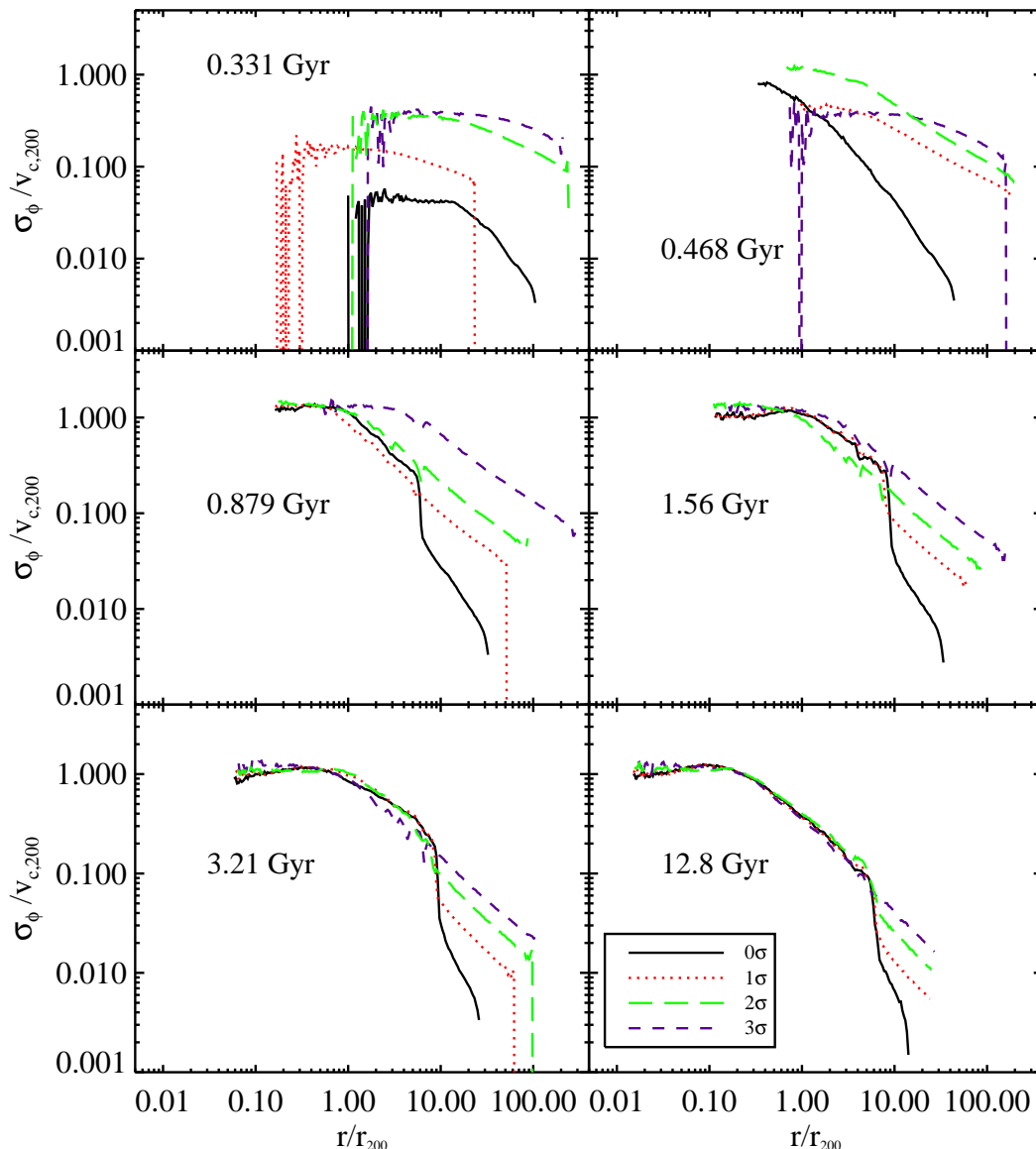


FIG. 5.— The evolution of the tangential velocity dispersion profile for each of the halos. Simulations represented are no dispersion (black solid line), 1σ dispersion (red dotted line), 2σ dispersion (green long-dashed line), and the 3σ dispersion (purple dashed line). The timestep is labelled on each panel.

The detailed behavior of the velocity dispersions in §3.2 can be simplified to a single measure of the velocity structure. A commonly used parameter for assessing the velocity structure of a halo is the global anisotropy:

$$2T_r/T_\phi \equiv \langle \sigma_r^2 \rangle / \langle \sigma_\phi^2 \rangle \quad (2)$$

where T_r and T_ϕ are kinetic energies of particles in the radial and tangential directions, respectively, and the averages are performed over the entire system. This quantity will be heavily weighted by the structure of the inner halo, which contains most of the halo mass. The global anisotropy parameter is intended to be used to describe spherical equilibrium systems, and we note that the most complete way to compute the anisotropy of an evolving, nonspherical halo is to make a complete three dimensional map of the velocity dispersion tensor. This quantity is difficult to represent, and we find that when we calculate the global anisotropy parameter

it closely follows the central velocity dispersion tensor. Thus we use the quantity $2T_r/T_\phi$ to characterize the typical anisotropy content at each timestep, even though our halos are evolving and deviate from spherical symmetry. Increasing values of the global anisotropy parameter indicate an increasing prevalence of radial orbits, and for a spherical equilibrium system, an increased likelihood of undergoing the ROI. Though a specific threshold for onset of the ROI has not been agreed upon, and depends moderately on the initial distribution function. Studies have found the threshold to be as low as $2T_r/T_\phi \sim 1.4$ (Barnes et al. 1986) or as high as 2.5 (Merritt & Aguilar 1985; Meza & Zamorano 1997) for equilibrium systems.

At each timestep, the values $\langle \sigma_r^2 \rangle$ and $\langle \sigma_\phi^2 \rangle$ for the entire halo are found by averaging the squares of the values of σ_r and σ_ϕ (see §3.2) from every radial bin normalized by the number of particles in each bin. The resulting values of $2T_r/T_\phi$ vs. time are presented in the up-

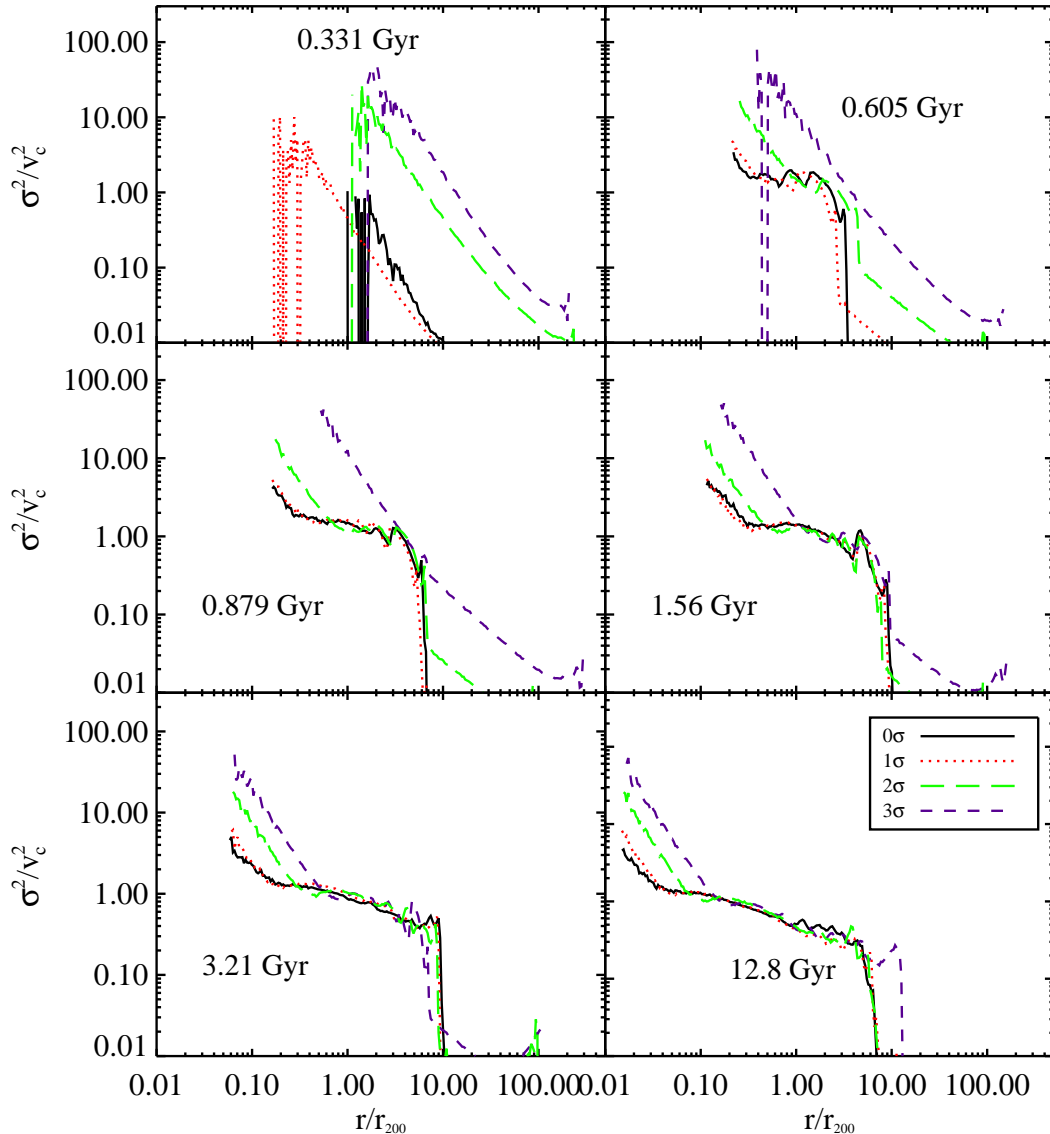


FIG. 6.— The ratio of the square of the velocity dispersion to the square of the circular velocity with radius, for each simulation at various times. Simulations represented are no dispersion (black solid line), 1σ dispersion (red dotted line), 2σ dispersion (green long-dashed line), and the 3σ dispersion (purple dashed line). The timestep is labelled in each panel. Instabilities grow when the velocity dispersion is low, and stabilize when the velocity dispersion becomes comparable to the circular velocity.

per panel of Figure 7, for the various initial velocity dispersions. At 0.5 Gyr, most halos have $2T_r/T_\phi \lesssim 0.5$ (the 0σ and 3σ radial-only halos have negligibly small tangential motions at this time, causing the value of $2T_r/T_\phi$ to be extremely large). However, the subsequent evolution of the profiles is quite different. The low velocity halos that undergo the ROI show strong increases in $2T_r/T_\phi$, which peaks at 0.6 Gyr, when the large infall velocities produce large values of $\langle \sigma_r^2 \rangle$. In contrast, the higher velocity dispersion halos (which do not appear to undergo the ROI) show only mild initial increases in $2T_r/T_\phi$, due to their larger tangential velocities. For every halo, these increases correspond directly to the time when each halo deviates noticeably from its original spherical shape.

Following the peak in $2T_r/T_\phi$, the onset of the ROI in the low- σ halos produces a bar which torques the halo particles. These torques produce larger tangential velocity dispersion, increasing $\langle \sigma_\phi^2 \rangle$ and thus decreasing

$2T_r/T_\phi$ to its final value of ~ 1.2 . Note that all halos converge to this final value, regardless of the presence of the ROI. We plot the time to 5 Gyr to better portray the evolution of the halos; after this time, the values of $2T_r/T_\phi$ are fairly constant throughout the remainder of the simulation.

Given the absence of the ROI triaxiality in the 2σ and 3σ halos, we can use the range between the peak values of the 1σ and 2σ runs to estimate the global anisotropy threshold for the ROI in our simulations. This estimate is a fairly loose one, since the 1σ halo is not exactly spherical, nor in equilibrium. Nonetheless, the resulting value is $2.0 < 2T_r/T_\phi < 2.97$ for our halos, the lower range of which is consistent with previous estimates for spherical equilibrium models.

The changes in anisotropy described above are not directly associated with virialization. The lower panel of Figure 7 shows the quantity $-2T/W$ vs. time, where T

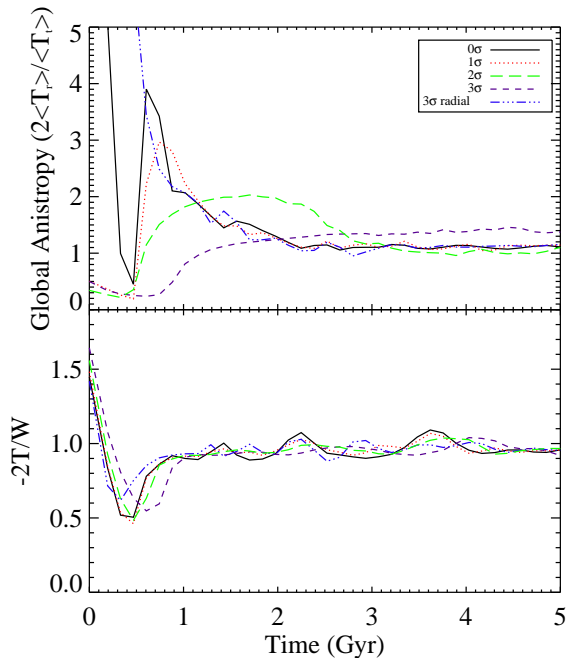


FIG. 7.— (*Upper Panel*) Global anisotropy of each halo versus time, showing no dispersion (black solid line), 1 σ dispersion (red dotted line), 2 σ dispersion (green long-dashed line), 3 σ dispersion (purple dashed line), and the 3 σ radial only dispersion (blue dot-dashed line). The ROI does not occur in systems with isotropic σ of 2 or higher. (*Lower Panel*) Ratio of twice the kinetic energy of the halo to the potential energy versus time. The ROI occurs on a different timescale than the virialization process.

and W are the sums of the kinetic and potential energies of each particle in a halo at each timestep. This quantity tracks the virialization process of the halo, which happens on a different timescale than the anisotropy evolution. Initially, each halo is a diffuse sphere expanding with the Hubble flow, so there is significant kinetic energy and modest potential energy. As the simulation proceeds, the particles reach turnaround and begin to collapse, at which point the total kinetic energy reaches a minimum along with the quantity $|2T/W|$. The ROI then proceeds directly after the primary collapse of the halo, as can be seen by the coeval increase in $2T_r/T_\phi$ (isotropization) with the rise of $|2T/W|$ (virialization) for each halo. However, isotropization due to the ROI continues after virialization, as can be seen in the broad peak in $2T_r/T_\phi$, which continues to evolve after $|2T/W|$ has reached its final value. These different timescales emphasize the distinctness of these two processes.

3.4. Anisotropy Profile

Closely related to the global anisotropy is the anisotropy parameter, β (Eqn 1). The parameter $\beta(r)$ is also defined for a spherical system, but we use it here as an approximate indication of the amount of radial motion in the orbits of our halos. When $\beta = 0$, the velocity dispersions σ_r and σ_ϕ are comparable and indicate an isotropic system. When $\beta = 1$, σ_r is much greater than σ_ϕ ; the orbits in such regions are dominated by infall, “shell-crossing”, and in general highly radial orbits. We examine β calculated in radial shells to characterize the typical orbits of particles in a given region. The resulting anisotropy profile $\beta(r)$ can be combined with the shape

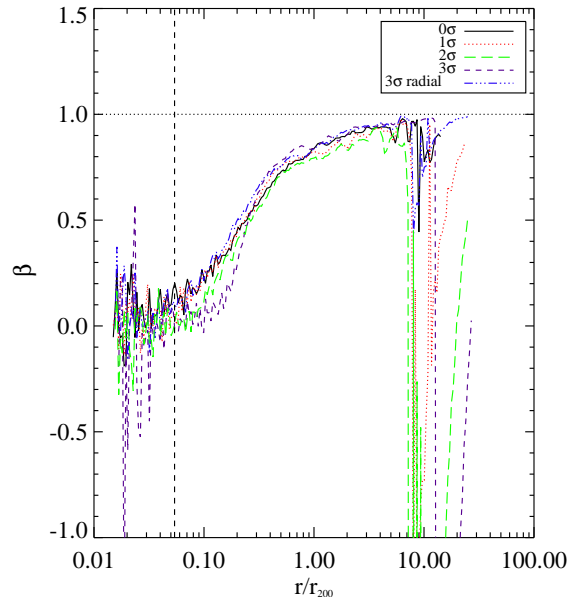


FIG. 8.— Anisotropy profiles for halos with no velocity dispersion (black solid line), 1 σ dispersion (red dotted line), 2 σ dispersion (green long-dashed line), 3 σ dispersion (purple dashed line), and the 3 σ radial only dispersion (blue dot-dashed line). The horizontal black dotted line marks $\beta = 1$ for reference, and the vertical black dashed line marks the softening length. All halos develop isotropic cores and radially-dominated outer regions, regardless of initial velocity dispersions.

information to isolate the dynamical effects taking place. We calculate $\beta(r)$ for each timestep using the values of σ_r and σ_ϕ described in §3.2.

Our halos all settle into a common final anisotropy profile, characterized by a roughly isotropic core surrounded by an anisotropic, radially-dominated outer region, as shown in Figure 8 and as noted in several other papers including Barnes et al. (2005). However, we find that this profile occurs regardless of initial velocity dispersion, and whether or not the ROI has taken place. We can explain this behavior as follows: the anisotropy of the outer regions is expected, since material at large radii predominately consists of inward and outward moving particles that began with a high gravitational potential, hence having large characteristic radial velocities. In the center, velocities are isotropic for one of two reasons: either the ROI has occurred, transferring radial motions to tangential, or the motions are dominated by the initial isotropic velocity dispersion imposed by the initial conditions. In the latter case, any increase in radial velocity dispersion due to infalling shells is counteracted by the increase in tangential velocities as particles attempt to conserve angular momentum in response to being pulled inward by the infalling material. Therefore, both the large and small radius behavior suggest that the behavior of $\beta(r)$ increasing from 0 to 1 should be quite typical, as we indeed find.

Although the overall shape of $\beta(r) = 0 \rightarrow 1$ is similar among all halos, we do see a slight signature of the ROI in the steepness with which $\beta(r)$ increases. The higher- σ halos have noticeably steeper transitions from $\beta(r) = 0 \rightarrow 1$, which could possibly be a result of the initial velocity dispersion dominating the core isotropy rather than the ROI.

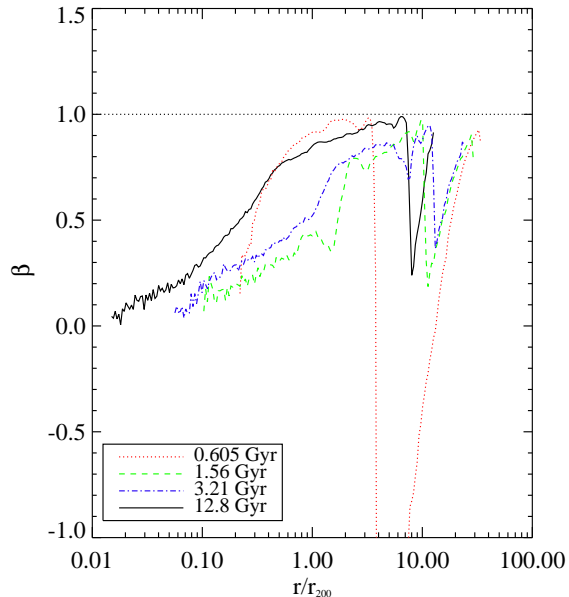


FIG. 9.— Evolution of the anisotropy profile with time for the high-resolution, 0σ halo. Red dotted line is $t = 0.605$ Gyr, green dashed line is $t = 1.56$ Gyr, blue dot-dashed line is $t = 3.21$ Gyr, black solid line is $t = 12.8$ Gyr. The black dotted line marks $\beta = 1$ for reference. Each profile is normalized to the virial radius at that timestep. The characteristic shape of $\beta(r)$ forms early and is maintained throughout the halo’s evolution.

It is important to point out that a triaxial halo core cannot be purely isotropic, though it appears so in Figure 8. This is due to our use of spherical radial bins to analyze a non-spherical system, and the fact that the standard-resolution halos do not have enough particles in the central region to properly resolve the orbital motions. An examination of the Cartesian velocity dispersion tensor of the central regions confirms that the core is nearly but not exactly isotropic. Our use of $\beta(r)$ as a measure of anisotropy is still very useful, however, as it effectively tracks large-scale changes in anisotropy with radius, as can be seen from the figures.

We track the time evolution of the anisotropy profile in Figure 9 for the high-resolution 0σ halo. The characteristic shape of the profile develops very early on as particles at small radii collapse and undergo mixing. At the first timestep shown, the ROI has just begun, causing the innermost particles to enter box orbits, while the rest of the halo is still dominated by radial infall (red dotted line). The near-isotropic core develops quickly and grows as more particles reach the center; by 1.6 Gyr, the ROI has operated on much of the center of the halo (green dashed line). The outermost regions consist of radially infalling material throughout the evolution of the halo. Note that the high-resolution halo has enough particles to resolve the orbital motions at the core. The $\beta(r)$ profile tends toward zero at small radii but an anisotropic component remains, due to the triaxiality of the halo.

The time evolution of the anisotropy profiles of the higher- σ halo is comparable to those of the “cold” halo, in that the cores of the halos become isotropic at early times. However, while these halos appear to develop similarly, the core isotropy comes about differently for each halo; the higher- σ halos have pre-existing isotropic orbits in the central region, preventing instabilities during

collapse and maintaining a central isotropic core. In contrast, the 0σ halo develops its isotropic core via the ROI. Therefore, the characteristic shape of the anisotropy profile is independent of the shape of the halo, and can be formed either when there is an existing isotropic velocity dispersion, or via such a mechanism as the ROI if the halo is dynamically cold.

This finding explains the results of Lu et al. (2006), who find that the universal $\gamma \sim -1$ inner halo density slope is formed for a variety of initial velocity dispersion distributions (i.e. radial, isotropic), particularly during an early “fast accretion” phase. Our Gaussian initial conditions are such that $\sim 90\%$ of the halo mass has a freefall time within 50% of the median. Thus our halos are likely to fall in the “fast accretion” regime of Lu et al. (2006). Note, however, that unlike Lu et al. (2006) we do not need to posit an additional source of isotropization for a core to be produced. The necessary isotropization occurs naturally either through the ROI or the conservation of angular momentum.

3.5. Density and Phase-Space Density Profiles

Halos with various velocity dispersions show similar structural properties, whether or not they undergo the ROI. Figure 10 plots the fully evolved density and phase-space density profiles of each standard-resolution halo. There is a noticeably shallower core in both the density and phase-space density profiles with higher σ . This effect was first reported by Merritt & Aguilar (1985) and is not surprising, considering the higher initial angular momenta characteristic of systems with large σ_ϕ . It is also important to recall from our tests in §2 that these medium-resolution simulations may not completely capture the properties of the halo core. So, while these results certainly make intuitive sense, high-resolution simulations are needed for confirmation within $0.05r_{200}$.

The evolution of the density and phase-space density profiles with time are shown in Figure 11 for the high-resolution, zero dispersion halo. Each profile is normalized to the virial radius at each corresponding timestep. The basic shape of each profile is formed after 1.5 Gyr of evolution and grows outward with radius as the halo collapses. The outermost radii have yet to collapse at the present time. The final density profile (top panel) is fit well out to $10r_{200}$ by an Einasto profile with $\alpha = 0.2$. The NFW profile with $c = 8.0$ gives a poorer fit at the outer edges (see Fig. 1, top panels).

Our halos exhibit a power-law in the phase-space density (represented by ρ/σ^3) with a slope of -1.7 that is relatively constant with time. The final halo power-law persists over ~ 2.5 decades in radius. The core phase-space density begins to develop its power-law structure at early times as well (Figure 11, bottom panel). These results are consistent with other simulations and do not seem to be affected by the ROI.

3.6. Scale Lengths

Barnes et al. (2005) developed a semi-analytic model of collapsing halos which includes a physical representation of the radial orbit instability. This model varies the initial perturbation velocities of the collapsing halo in such a way that an isotropic core is produced, with orbits becoming more anisotropic with increasing radius.

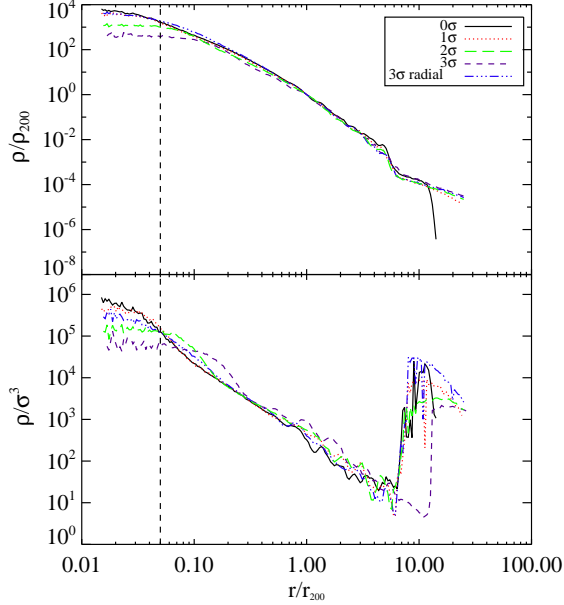


FIG. 10.— Fully evolved density and phase-space density profiles for halos with no velocity dispersion (black solid line), 1σ dispersion (red dotted line), 2σ dispersion (green long-dashed line), 3σ dispersion (purple dashed line), and the 3σ radial only dispersion (blue dot-dashed line). The vertical dashed line marks the radius below which softening and resolution begin to affect the profiles. All of the profiles are very similar, except that halos with higher velocity dispersion have shallower cores.

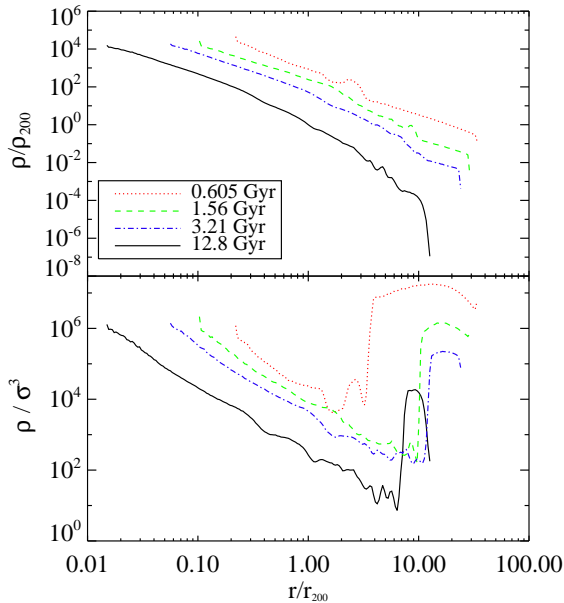


FIG. 11.— Evolution of the density and phase-space density profiles with time for the high-resolution, 0σ halo. Red dotted line is $t = 0.605$ Gyr, green dashed line is $t = 1.56$ Gyr, blue dot-dashed line is $t = 3.21$ Gyr, black solid line is $t = 12.8$ Gyr. All density curves are normalized to ρ_{200} at $t = 12.8$ Gyr to better show the density profile evolution. The profile shapes are set early on and evolve radially outwards with time.

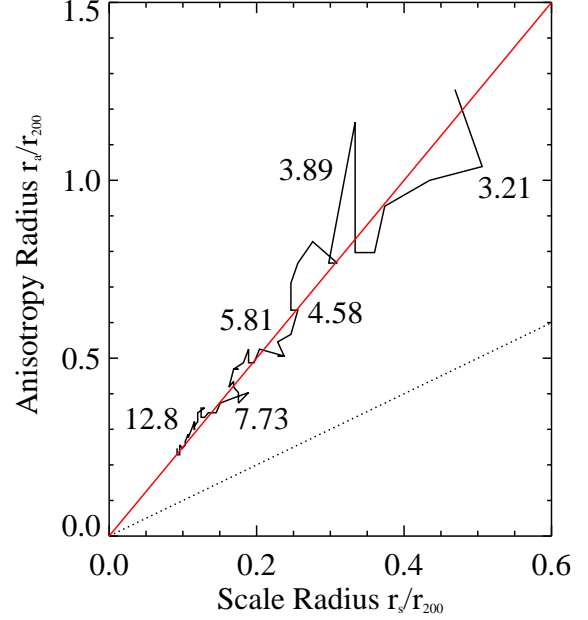


FIG. 12.— Anisotropy radius (r_a/r_{200}) versus density scale radius (r_s/r_{200}) for the standard resolution, 0σ halo. These radii appear to be correlated with a slope of 2.5 (red line). The semi-analytic model of Barnes et al. (2005) gives a slope of ~ 1 (dotted line). Numbers on the plot indicate the time in Gyr at that particular point.

This model produces realistic NFW density profiles and power-law phase-space density profiles for a series of halos. In addition, the model shows a direct correlation between the anisotropy radius (r_a), defined as the radius where $\beta = 0.5$, and the density scale length (r_s , here defined as the radius where $\gamma = -2$). This correlation is assumed to be a result of the ROI acting to flatten the density cusp by torquing the orbits of the inner halo particles and forming an isotropic core.

While we showed in §3.3 that the characteristic anisotropy profile is not always due to the ROI, we still expect a correlation between r_a and r_s . Within r_a , tangential velocities are large, and the resulting high angular momenta should keep particles from penetrating the very center of the halo. This angular momentum barrier should lead to a flatter core whose size r_s is physically related to the size of the isotropic region.

To test the conclusion presented in Barnes et al. (2005), in Figure 12 we plot the relation between r_a and r_s as a function of time for the standard-resolution, zero-dispersion halo. The numbers on the figure indicate the time in Gyr at that particular point. While our N-body simulations do not confirm that the radii are equal, the two scale lengths are clearly proportional to each other. While there is considerable scatter, the points gravitate toward a line with slope ~ 2.5 , suggesting that the anisotropy radius and the scale radius have some connection in their development. One reason for the difference in the slope of our relation versus that of Barnes et al. (2005) could be their assumption that the ROI does not change the energies of the particles, only the angular momenta. Our N-Body simulations allow for both of these quantities to change, allowing for a more accurate portrayal of the ROI. Thus the possibility remains that the ROI is the mechanism that produces the

characteristic anisotropy profile for a “cold” collapsing system.

4. CONCLUSIONS

We have conducted N-body simulations of a variety of isolated, collapsing dark matter halos to investigate the role of the radial orbit instability on the final halo structure. The ROI plays a role in determining the eventual shape, density profile, and phase-space density profile of a halo. The ROI is suppressed in halos with isotropic initial velocity dispersions, but halos with purely radial velocity dispersions appear to undergo the instability.

Many numerical simulations have produced triaxial dark matter halos (Frenk et al. 1988; Warren et al. 1992; Thomas et al. 1998; Jing & Suto 2002). Observational evidence for triaxial halos is also appearing, from low surface brightness and dwarf galaxies (Bureau et al. 1999; Simon et al. 2005; Hayashi et al. 2006) and from galaxy clusters (Oguri et al. 2003; Lee & Suto 2004). Such evidence for the existence of triaxial halos strengthens our hypothesis that dynamically cold halos undergo the ROI during collapse and therefore obtain a triaxial shape. A warmer system would not become unstable and would have a final shape that is too spherical to explain the observed structures. While the linear overdensities in the early universe are themselves triaxial, not spherical (Bardeen et al. 1986), and hence also contribute to the triaxiality of the resulting halos, the ROI significantly affects the inner, observable parts of the halo.

The characteristic anisotropy profile seen in all of our halos, and in others in the literature, is independent of the ROI, and appears to be a result of the general process of halo collapse. However, in cases where the ROI does occur, it is likely to be the cause of such profiles. In these cases, there is a link between the density scale radius and the anisotropy radius, indicating a causal relation between the two. Further semi-analytic and N-Body

simulations may help to clarify this potential connection.

While simulations of isolated collapsing halos are useful for trying to understand the effects of the ROI, it is well known that in realistic cosmological settings, halos form hierarchically. Their evolution is marked by periods of gentle accretion, typically in the form of minor mergers, occasionally punctuated by major mergers. To understand the role and relevance of the ROI in halos evolving in this way, we are presently in the process of carrying out and analyzing simulations of halos subject to controlled major and minor mergers (cf. (Poole et al. 2007)). At this early stage, we are finding that the complex dynamics at play during major mergers makes it difficult to ascertain straightforwardly whether the ROI plays a significant role during the subsequent relaxation process; a priori, we would speculate that it does not. However, there are indications that the ROI is operational during periods of quiescent accretion, by acting upon nearly radial tidal streams associated with disrupting subhalos, which become isotropic. We speculate that the weak tides induced by these weak structures in fact both seeds and reinforces the instability.

JMB thanks the NSF Graduate Research Fellowship Program. JMB, LLRW, AB, JJD, CGA, EIB, and RWM would like to acknowledge NSF grant AST-0307604. JJD was also supported by a Wyckoff Faculty Fellowship at the University of Washington. AB acknowledges support from NSERC (Canada)’s Discovery Grant Program as well as the Leverhulme Trust for awarding him a Leverhulme Visiting Professorship. Computing resources were made possible through a grant from the Student Technology Fee of the University of Washington. The authors thank Andrew West for useful insights and the anonymous referee for helpful suggestions which improved the paper.

REFERENCES

- Ascibar, Y., Yepes, G., Gottlöber, S., & Müller, V. 2004, *MNRAS*, 352, 1109
- Austin, C. G., Williams, L. L. R., Barnes, E. I., Babul, A., & Dalcanton, J. J. 2005, *ApJ*, 634, 756
- Babul, A., & Starkman, G. D. 1992, *ApJ*, 401, 28
- Bardeen, J. M., Bond, J. R., Kaiser, N., & Szalay, A. S. 1986, *ApJ*, 304, 15
- Barnes, E. I., Williams, L. L. R., Babul, A., & Dalcanton, J. J. 2005, *ApJ*, 634, 775
- Barnes, J., Hut, P., & Goodman, J. 1986, *ApJ*, 300, 112
- Bertschinger, E. 1985, *ApJS*, 58, 39
- Bullock, J. S., Dekel, A., Kolatt, T. S., Kravtsov, A. V., Klypin, A. A., Porciani, C., & Primack, J. R. 2001, *ApJ*, 555, 240
- Bureau, M., Freeman, K. C., Pfizner, D. W., & Meurer, G. R. 1999, *AJ*, 118, 2158
- Carlberg, R. G. et al. 1997, *ApJL*, 485, L13+
- Cole, S., & Lacey, C. 1996, *MNRAS*, 281, 716
- Dalcanton, J. J., & Hogan, C. J. 2001, *ApJ*, 561, 35
- Dehnen, W., & McLaughlin, D. E. 2005, *MNRAS*, 363, 1057
- Dejonghe, H., & Merritt, D. 1988, *ApJ*, 328, 93
- Dubinski, J., & Carlberg, R. G. 1991, *ApJ*, 378, 496
- Frenk, C. S., White, S. D. M., Davis, M., & Efstathiou, G. 1988, *ApJ*, 327, 507
- Fukushige, T., & Makino, J. 2001, *ApJ*, 557, 533
- Gott, J. R. I. 1975, *ApJ*, 201, 296
- Gunn, J. E. 1977, *ApJ*, 218, 592
- Gunn, J. E., & Gott, J. R. I. 1972, *ApJ*, 176, 1
- Hansen, S. H., & Moore, B. 2006, *New Astronomy*, 11, 333
- Hansen, S. H., Moore, B., Zemp, M., & Stadel, J. 2006, *Journal of Cosmology and Astro-Particle Physics*, 1, 14
- Hayashi, E., Navarro, J. F., & Springel, V. 2006, *ArXiv Astrophysics e-prints*
- Hiotelis, N. 2002, *AAP*, 382, 84
- Huss, A., Jain, B., & Steinmetz, M. 1999, *ApJ*, 517, 64
- Jing, Y. P., & Suto, Y. 2002, *ApJ*, 574, 538
- Le Delliou, M., & Henriksen, R. N. 2003, *AAP*, 408, 27
- Lee, J., & Suto, Y. 2004, *ApJ*, 601, 599
- Lu, Y., Mo, H. J., Katz, N., & Weinberg, M. D. 2006, *MNRAS*, 368, 1931
- MacMillan, J. D., Widrow, L. M., & Henriksen, R. N. 2006, *ApJ*, 653, 43
- Merritt, D., Navarro, J. F., Ludlow, A., & Jenkins, A. 2005, *ApJL*, 624, L85
- Merritt, D. 1999, *PASP*, 111, 129
- Merritt, D., & Aguilar, L. A. 1985, *MNRAS*, 217, 787
- Meza, A., & Zamorano, N. 1997, *ApJ*, 490, 136
- Moore, B., Quinn, T., Governato, F., Stadel, J., & Lake, G. 1999, *MNRAS*, 310, 1147
- Navarro, J. F., Frenk, C. S., & White, S. D. M. 1996, *ApJ*, 462, 563
- . 1997, *ApJ*, 490, 493
- Navarro, J. F. et al. 2004, *MNRAS*, 349, 1039
- Oguri, M., Lee, J., & Suto, Y. 2003, *ApJ*, 599, 7
- Poole, G. B., Babul, A., McCarthy, I. G., Fardal, M. A., Bildfell, C. J., Quinn, T., & Mahdavi, A. 2007, *MNRAS*, 380, 437
- Ryden, B. S., & Gunn, J. E. 1987, *ApJ*, 318, 15

- Simon, J. D., Bolatto, A. D., Leroy, A., Blitz, L., & Gates, E. L. 2005, *ApJ*, 621, 757
- Spergel, D. N. et al. 2007, *ApJS*, 170, 377
- Stadel, J. G. 2001, Ph.D. Thesis
- Taylor, J. E., & Navarro, J. F. 2001, *ApJ*, 563, 483
- Thomas, P. A. et al. 1998, *MNRAS*, 296, 1061
- Trenti, M., & Bertin, G. 2006, *ApJ*, 637, 717
- van den Bosch, F. C. 2002, *MNRAS*, 331, 98
- Wadsley, J. W., Stadel, J., & Quinn, T. 2004, *New Astronomy*, 9, 137
- Warren, M. S., Quinn, P. J., Salmon, J. K., & Zurek, W. H. 1992, *ApJ*, 399, 405
- Weinberg, M. D. 1991, *ApJ*, 368, 66
- Williams, L. L. R., Babul, A., & Dalcanton, J. J. 2004, *ApJ*, 604, 18